Development of an Applied Field Magnetoplasmadynamic Thruster Design Supported by Numerical Simulations at IRS

IEPC-2005-059

Presented at the 29th International Electric Propulsion Conference, Princeton University, October 31 – November 4, 2005

Daniel Haag*, Monika Auweter-Kurtz†, Markus Fertig‡ *and* Helmut Kurtz§
Universität Stuttgart, Institut für Raumfahrtsysteme (IRS), Pfaffenwaldring 31, 70550 Stuttgart, Germany

In this paper an overview is given on a numerical simulation program for applied field magnetoplasmadynamic thrusters which is currently under development at the Institute of Space Systems (IRS). The simulation code for argon plasma flows in thermal and chemical non-equilibrium uses an axisymmetric finite volume scheme on unstructured, adaptive meshes. The external magnetic field is taken into account employing the vector potential formulation. Azimuthal velocity and magnetic field are handled by a quasi-three dimensional approach with vanishing azimuthal derivatives. Besides the numerical analysis, a radiation-cooled laboratory model of an applied field magnetoplasmadynamic thruster is under development at IRS. The modular design allows adjustments of the thruster to find an optimized thruster geometry based on numerical and experimental results.

Nomenclature

$\vec{A}$	=	Vector potential, Vsm^{-1}
ΔA	=	Finite volume cell area, m^2
$\vec{B}$	=	Magnetic induction, T
$\vec{E}$	=	Electric field, Vm^{-1}
e	=	Energy density, Jm^{-3}
$\vec{f}$	=	Flux vector, Nm^{-2} resp. Wm^{-2}
I	=	Current, A
$\vec{j}$	=	Diffusion flux, $\mathrm{m}^{-2}\mathrm{s}^{-1}$
$\vec{j}$	=	Electric current density, Am^{-2}
k	=	Reaction rate, $\mathrm{m}^3\mathrm{s}^{-1}$
n	=	Particle density, m^{-3}
p	=	Pressure, Pa
q	=	Source term, Nm^{-3} resp. Wm^{-3}

* Scientist, Institute of Space Systems, haag@irs.uni-stuttgart.de.
† Professor, Deputy Director IRS, Head of Dept. Space Transportation Technology, auweter@irs.uni-stuttgart.de.
‡ Scientist, Institute of Space Systems, fertig@irs.uni-stuttgart.de.
§ Research Engineer, Institute of Space Systems, kurtz@irs.uni-stuttgart.de.

r = Radial coordinate, m
T = Temperature, K
t = Time, s
$\vec{v}$ = Velocity, ms^{-1}
Z = Charge number, -
z = Axial coordinate, m
α = Energy transfer coefficient, $\mathrm{Wm}^{-3}\mathrm{K}$
β = $1/(en_e)$, $\mathrm{m}^3\mathrm{C}^{-1}$
λ = Thermal conductivity, $\mathrm{Wm}^{-1}\mathrm{K}^{-1}$
ρ = Density, kgm^{-3}
σ = Electric conductivity, $\Omega^{-1}\mathrm{m}^{-1}$
τ = Viscous stress, Nm^{-2}
τ = Mean free flight time, s
φ = Azimuthal, -
χ = Ionization energy, J
ω = Reaction source term, $\mathrm{m}^{-3}\mathrm{s}^{-1}$
ω = Gyration frequency, s^{-1}

Subscripts

A = Anode
b = Backward
c = Coil
D = Diffusion
e = Electron
f = Forward
h = Heavy particle
i = I-fold ionized species
$invisc$ = Inviscid
m = Centre of mass
r = Radial
$visc$ = Viscous
z = Axial
φ = Azimuthal

Physical constants

e = $1{,}60219 \cdot 10^{-19}$ As
k = $1{,}38062 \cdot 10^{-23}$ JK^{-1}
μ_0 = $4\pi \cdot 10^{-7}$ $\mathrm{VsA}^{-1}\mathrm{m}^{-1}$

I. Introduction

Applied field magnetoplasmadynamic (AF-MPD) thrusters in the power range 5-100 kW are promising devices for orbit control systems of large satellites because of their high specific impulse, thrust density and efficiency. Furthermore, AF-MPD thrusters at higher power levels appear to be excellently suited for interplanetary space missions like crewed and uncrewed Mars missions.[1] Several laboratory devices and prototypes of AF-MPD thrusters have been developed and theoretically and experimentally investigated in Germany,[2,3] the USA,[4] the former USSR[5] and Japan[6,7] during the last three decades. With one of the best devices, the applied field thruster DFVLR-X16 developed at DLR Stuttgart, a thrust of 251 mN, an effective exit velocity of 36 km/s and an efficiency of 38.8 % was achieved with an applied magnetic field of 0.6 T.[8]

The step to flight-qualified AF-MPD thrusters has not been taken yet. One reason for this status is the low pressure needed for ground tests of AF-MPD thrusters (tank pressure lower than 0.1-0.01 Pa). Measurements have shown that specific thrust (F/I) increases as tank pressure is reduced.[9] The saturation point of specific thrust had not been achieved in these tests. Also, current stream lines are extended far outside the thruster with increasing strength of the applied magnetic field and decreasing ambient pressure. To avoid interaction with the wall, the vacuum facilities must be adequately dimensioned and made of non-magnetic steel. The optimization of the devices is difficult because AF-MPD thrust depends on plasma parameters, which depend on each other, and on their distribution. The complex acceleration processes are not thoroughly understood yet. Therefore, efficient numerical simulation tools are needed to gain experience and to support further development.

In 1996, the Institute of Space Systems (IRS) proposed an experimental platform for an AF-MPD thruster on the International Space Station (ISS), which could help to explore the acceleration mechanisms and clarify environmental influences.[10] One of the first steps for testing an AF-MPD device in space is the development of an optimized thruster design for a power level of 10-20 kW. This requires pre-qualification of a thruster model in ground test facilities. Supported by the German Research Foundation DFG (Deutsche Forschungsgemeinschaft) a program for numerical simulations of AF-MPD thrusters is currently under development at IRS. The simulation software SAMSA (Self and applied field MPD thruster simulation algorithm) is based on a numerical code that has been developed and was qualified at IRS for the simulation of self-field MPD thrusters.[11] SAMSA is intended to be used to achieve a better understanding of the basic plasmaphysical processes, which lead to the acceleration of the propellant, and to optimize the thruster and electrode geometry and particularly the configuration of the applied magnetic field of an AF-MPD thruster.

Beyond the numerical simulations, the DFG research project also includes the development and experimental investigation of an AF-MPD laboratory thruster to gain experience by comparing numerical and experimental results. At IRS, a thruster test facility, which is equipped with a diffusion pump system to achieve high vacuum, is especially suitable for testing of this thruster.

In the following sections of this paper an overview on the principles of operation of AF-MPD thrusters and the physical model and computational methods implemented in SAMSA is given. Also, the first numerical results and a characterization of the laboratory thruster used for experimental investigations at IRS are shown.

II. Physical properties of AF-MPD thrusters

The principle design of an AF-MPD thruster is illustrated in Fig. 1. It consists of a central cathode and a coaxial anode at the end of a nozzle-like configuration. The applied magnetic field is created by coaxial arranged coils or permanent magnets.

Acceleration and energy conversion mechanisms of AF-MPD thrusters can be derived from the generalized Ohm's law and the corresponding energy equation:[2]

$$\begin{aligned} \vec{j} &= \sigma\left(\vec{E} + \vec{v}\times\vec{B}\right) - \frac{\omega_e \tau_e}{\left|\vec{B}\right|}\left(\vec{j}\times\vec{B}\right) + \frac{1}{en_e}\nabla p_e \,, \\ \vec{j}\cdot\vec{E} &= \frac{\left|\vec{j}\right|^2}{\sigma} + \vec{v}\left(\vec{j}\times\vec{B}\right) - \frac{1}{en_e}\vec{j}\nabla p_e \,. \end{aligned} \tag{1}$$

Four main acceleration mechanisms are known to be effective:[1,2]

1) Joule heating and thermal expansion through a nozzle.
2) Interaction of discharge current arc and self-induced azimuthal magnetic field leads to axial and radial acceleration.
3) Interaction of discharge current and applied magnetic field results in azimuthal force that puts plasma into rotation. The rotational energy can be partly converted to axial acceleration downstream.
4) Interaction of induced azimuthal current (Hall current) and applied magnetic field produces axial and radial Lorentz forces.

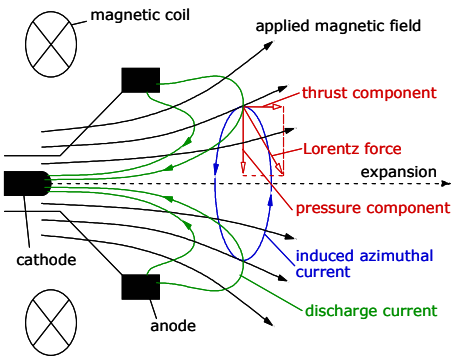

Figure 1. Principle design of an AF-MPD thruster with coaxial magnetic field.

The formation of high azimuthal currents is very important to achieve high thrust. Particle collision rates have to be low to get high azimuthal currents. Therefore, the Hall parameter can be seen as characteristic parameter for AF-MPD thrusters:[12]

$$\omega_e \tau_e = \frac{\sigma \left| \vec{B} \right|}{e n_e} \propto \frac{\left| \vec{B} \right| T_e^{5/2}}{p_e}. \tag{2}$$

Equation 2 indicates that strong magnetic field, high temperature and low pressure are necessary to gain high thrust in AF-MPD thrusters.

The strong applied magnetic field leads to reduced electrical conductivity perpendicular to the magnetic field:

$$\sigma_\perp = \frac{\sigma_\parallel}{1 + (\omega_e \tau_e)^2}. \tag{3}$$

Because of the anisotropic electrical conductivity, the current stream lines are extended far outside the thruster ("magnetic nozzle effect").[12] Therefore, for numerical simulations of AF-MPD thrusters the calculation domain has to be extended far downstream from the thruster. Also, this region has to be included into the calculation to allow the conversion of rotational energy into axial acceleration of the propellant as mentioned above.

III. Physical Model for Numerical Simulations

Due to axisymmetric AF-MPD thruster geometries, the plasma flow inside the calculation domain is supposed to be axisymmetric as well. Hence, the conservation equations are used in a two-dimensional form using cylindrical coordinates. Considering all relevant acceleration mechanisms, azimuthal components have to be included into the model for electrodynamic variables, the plasma velocity and momentum. For this reason, a quasi-three dimensional approach is used with azimuthal derivatives set to zero, i.e.:

$$\operatorname{div} \begin{pmatrix} a_r \\ a_\varphi \\ a_z \end{pmatrix} \equiv \frac{1}{r} \frac{\partial (r a_r)}{\partial r} + \frac{\partial a_z}{\partial z} \equiv \operatorname{div} \begin{pmatrix} a_r \\ a_z \end{pmatrix}. \tag{4}$$

Argon is used as propellant because of its low specific ionization level.[8] Assuming continuum flow, the argon plasma is considered as quasineutral two-fluid plasma in thermal and chemical nonequilibrium (up to 6-fold ionized argon). The transport coefficients of argon, which are required by the conservation equations, are calculated according to Heiermann and Auweter-Kurtz.[11,13]

No turbulence is considered due to strong viscous dissipation in the hot plasma and low pressure level in AF-MPD thrusters.

A. Conservation of mass

Conservation of mass is expressed as balance of particle densities for each heavy particle species:

$$\frac{\partial n_i}{\partial t} = -\operatorname{div}\left(n_i \vec{v}\right) - \operatorname{div}\, \vec{j}_{D,i} + \omega_i \,. \tag{5}$$

Diffusion fluxes $\vec{j}_{D,i}$ are computed with formulas from Heiermann and Auweter-Kurtz.[11,13] A conservation equation for electron particle density is not needed because of quasineutral assumption.

The chemical source term ω_i includes electron impact ionization and three-body recombination:

$$\begin{aligned}
\omega_0 &= -n_0 n_e k_{f,1} + n_1 n_e^2 k_{b,1} \,, \\
\omega_i &= +n_{i-1} n_e k_{f,i} - n_i n_e^2 k_{b,i} - n_i n_e k_{f,i+1} + n_{i+1} n_e^2 k_{b,i+1} \,, \\
\omega_6 &= +n_5 n_e k_{f,6} - n_6 n_e^2 k_{b,6} \,.
\end{aligned} \tag{6}$$

The forward reaction rates $k_{f,i}$ and backward reaction rates $k_{b,i}$ are calculated according to Heiermann and Auweter-Kurtz.[11,13]

B. Conservation of momentum

The conservation equation for radial momentum is given by

$$\begin{aligned}
&\frac{\partial\left(\rho v_r\right)}{\partial t} = -\operatorname{div}\, \vec{f}_{invisc}^{\rho v_r} - \operatorname{div}\, \vec{f}_{visc}^{\rho v_r} + q^{\rho v_r} \quad \text{, where} \\
&\vec{f}_{invisc}^{\rho v_r} = \begin{pmatrix} \rho v_r^2 + p_h + p_e \\ \rho v_r v_z \end{pmatrix} \text{ is the inviscid flux,} \\
&\vec{f}_{visc}^{\rho v_r} = \begin{pmatrix} -\tau_{rr} \\ -\tau_{rz} \end{pmatrix} \text{ is the viscous flux and} \\
&q^{\rho v_r} = \frac{\rho v_\varphi^2 + p_h + p_e - \tau_{\varphi\varphi}}{r} + \left(j_\varphi B_z - j_z B_\varphi\right) \text{ is the source term.}
\end{aligned} \tag{7}$$

The first term of the source term arises from using cylindrical coordinates.[14] The second term describes the effect of electromagnetic interaction.

The conservation equation of azimuthal momentum is given by

$$\begin{aligned}
&\frac{\partial\left(\rho v_\varphi\right)}{\partial t} = -\operatorname{div}\, \vec{f}_{invisc}^{\rho v_\varphi} - \operatorname{div}\, \vec{f}_{visc}^{\rho v_\varphi} + q^{\rho v_\varphi} \quad \text{, where} \\
&\vec{f}_{invisc}^{\rho v_\varphi} = \begin{pmatrix} \rho v_r v_\varphi \\ \rho v_\varphi v_z \end{pmatrix} \text{ is the inviscid flux,} \\
&\vec{f}_{visc}^{\rho v_\varphi} = \begin{pmatrix} -\tau_{r\varphi} \\ -\tau_{\varphi z} \end{pmatrix} \text{ is the viscous flux and} \\
&q^{\rho v_\varphi} = \frac{\tau_{r\varphi} - \rho v_r v_\varphi}{r} + \left(j_z B_r - j_r B_z\right) \text{ is the source term.}
\end{aligned} \tag{8}$$

The conservation equation of axial momentum is given by

$$
\begin{aligned}
&\frac{\partial(\rho v_z)}{\partial t} = -\operatorname{div} \vec{f}_{invisc}^{\rho v_z} - \operatorname{div} \vec{f}_{visc}^{\rho v_z} + q^{\rho v_z} \quad \text{, where} \\
&\vec{f}_{invisc}^{\rho v_z} = \begin{pmatrix} \rho v_r v_z \\ \rho v_z^2 + p_h + p_e \end{pmatrix} \text{ is the inviscid flux,} \\
&\vec{f}_{visc}^{\rho v_z} = \begin{pmatrix} -\tau_{rz} \\ -\tau_{zz} \end{pmatrix} \text{ is the viscous flux and} \\
&q^{\rho v_z} = \left(j_r B_\varphi - j_\varphi B_r \right) \text{ is the source term.}
\end{aligned}
\tag{9}
$$

The viscous stresses are given by

$$
\begin{aligned}
&\tau_{rr} = \frac{2}{3}\mu\left(2\frac{\partial v_r}{\partial r} - \frac{v_r}{r} - \frac{\partial v_z}{\partial z}\right), \quad \tau_{\varphi\varphi} = \frac{2}{3}\mu\left(2\frac{v_r}{r} - \frac{\partial v_r}{\partial r} - \frac{\partial v_z}{\partial z}\right), \quad \tau_{zz} = \frac{2}{3}\mu\left(2\frac{\partial v_z}{\partial z} - \frac{v_r}{r} - \frac{\partial v_r}{\partial r}\right), \\
&\tau_{r\varphi} = \tau_{\varphi r} = \mu\left(\frac{\partial v_\varphi}{\partial r} - \frac{v_\varphi}{r}\right), \qquad \tau_{rz} = \tau_{zr} = \mu\left(\frac{\partial v_z}{\partial r} - \frac{\partial v_r}{\partial z}\right) \text{ and } \quad \tau_{\varphi z} = \tau_{z\varphi} = \mu\frac{\partial v_\varphi}{\partial z}.
\end{aligned}
\tag{10}
$$

C. Conservation of energy

With the equation of state for heavy particle pressure

$$
p_h = n_h k T_h \,, \tag{11}
$$

heavy particle energy e_h, which is composed of translatory and kinetic energy, is defined as

$$
e_h = \frac{3}{2} n_h k T_h + \frac{1}{2}\rho\left|\vec{\mathrm{v}}\right|^2 \quad . \tag{12}
$$

The conservation equation for heavy particle energy is given by

$$
\begin{aligned}
&\frac{\partial e_h}{\partial t} = -\operatorname{div} \vec{f}_{invisc}^{e_h} - \operatorname{div} \vec{f}_{visc}^{e_h} + q^{e_h} \quad \text{, where} \\
&\vec{f}_{invisc}^{e_h} = \left(\left(e_h + p_h + p_e\right) \begin{pmatrix} v_r \\ v_z \end{pmatrix} \right) \text{ is the inviscid flux,} \\
&\vec{f}_{visc}^{e_h} = \begin{pmatrix} -\tau_{rr} v_r - \tau_{r\varphi} v_\varphi - \tau_{rz} v_z - \lambda_h \dfrac{\partial T_h}{\partial r} \\ -\tau_{rz} v_r - \tau_{\varphi z} v_\varphi - \tau_{zz} v_z - \lambda_h \dfrac{\partial T_h}{\partial z} \end{pmatrix} \text{ is the viscous flux and} \\
&q^{e_h} = p_e \operatorname{div} \vec{v} + \vec{v}\left(\vec{j} \times \vec{B}\right) + \sum_{i=0}^{6} n_{hi} n_e \alpha_{ie} \left(T_e - T_h\right) \text{ is the source term.}
\end{aligned}
\tag{13}
$$

The flux vector $\vec{f}_{visc}^{\rho v_z}$ includes fluxes created by viscous forces and heat conduction of heavy particles. In the source term q^{e_h} the first term arises because the electron pressure is included in the inviscid flux $\vec{f}_{invisc}^{e_h}$, the second term describes the power due to Lorentz force and the last term describes energy transfer between electrons and heavy particles.

With electron pressure defined as

$$
p_e = n_e k T_e \tag{14}
$$

and electron energy

$$e_e = \frac{3}{2} n_e k T_e \,, \tag{15}$$

the conservation equation of electron energy is given by

$$\frac{\partial e_e}{\partial t} = -\operatorname{div}\left(e_e \vec{v}_e\right) - p_e \operatorname{div} \vec{v}_e - \operatorname{div}\left(\frac{3}{2} k T_e \vec{j}_{D,e}\right) + \operatorname{div}\left(\lambda_e \nabla T_e\right) + \sum_{i=1}^{6} n_e n_i \alpha_{ei} \left(T_h - T_e\right) + \frac{\left|\vec{j}\right|^2}{\sigma} - \sum_{i=0}^{5} \omega_{i+1} \chi_{i \to i+1} \,. \tag{16}$$

The terms on the right hand side of Eq. 16 describe convective transport caused by electron velocity $\vec{v}_e$, deformation of an electron fluid element due to electron pressure, transport caused by diffusion flux $\vec{j}_{D,e}$, electron heat conduction, energy transfer between electrons and heavy particles, Ohmic heating and energy balance due to ionization.

By defining the current density

$$\vec{j} = e n_e \left(\vec{v} - \vec{v}_e\right) \tag{17}$$

and utilizing the assumption of quasineutral plasma, Eq. 16 can be transformed to

$$\begin{aligned} \frac{\partial e_e}{\partial t} = & -\operatorname{div}\left(e_e \vec{v}\right) - p_e \operatorname{div} \vec{v} + \frac{5}{2} \frac{k}{e} \vec{j} \nabla T_e - \frac{1}{e n_e} \vec{j} \nabla p_e - \operatorname{div}\left(\frac{3}{2} k T_e \sum_{i=1}^{6} Z_i \vec{j}_{D,i}\right) \\ & + \operatorname{div}\left(\lambda_e \nabla T_e\right) + \sum_{i=1}^{6} n_e n_i \alpha_{ei} \left(T_h - T_e\right) + \frac{\left|\vec{j}\right|^2}{\sigma} - \sum_{i=0}^{5} \omega_{i+1} \chi_{i \to i+1} \,. \end{aligned} \tag{18}$$

D. Conservation of the magnetic field

Using Ohm's law for plasmas (Eq. 1) and the Maxwell equations,[15,16] conservation equations for the axial, radial and azimuthal components of the magnetic field can be achieved. In self-field MPD thrusters only the azimuthal component of these conservation equations is necessary to describe the arc discharge between cathode and anode and the induced magnetic field.[11,13]

In AF-MPD thrusters the axial and radial components are additionally needed to include the influence of the applied magnetic field and induced azimuthal current density. These influences are described employing the vector potential formulation:[16]

$$\vec{B}\Big|_{r,z} = \begin{pmatrix} B_r \\ 0 \\ B_z \end{pmatrix} = \operatorname{rot} \begin{pmatrix} 0 \\ A \\ 0 \end{pmatrix}. \tag{19}$$

By using the vector potential formulation, the computation of boundary values influenced by the magnetic field, which is created by solenoidal coil currents, and the induced azimuthal currents can be managed, as will be shown in section IV below. The zero divergence constraint is also satisfied for the quasi-three dimensional approach ($\partial / \partial \varphi = 0$):

$$\operatorname{div} \begin{pmatrix} 0 \\ B_\varphi \\ 0 \end{pmatrix} + \operatorname{div} \left(\operatorname{rot} \begin{pmatrix} 0 \\ A \\ 0 \end{pmatrix} \right) = 0 \,. \tag{20}$$

The conservation equation for the azimuthal component of the magnetic field is given by

$$\frac{\partial B_\varphi}{\partial t} = -\mathrm{div}\left(B_\varphi \vec{v} - v_\varphi \vec{B}\right) - \frac{v_\varphi B_r - v_r B_\varphi}{r} - \mathrm{rot}\left(\frac{\mathrm{rot}\,\vec{B}\big|_\varphi}{\mu_0 \sigma} - \frac{\beta}{\mu_0} \mathrm{rot}\,\vec{B} \times \vec{B} - \beta \nabla p_e \right)\Bigg|_\varphi \quad \text{where } \beta = \frac{1}{e n_e}. \tag{21}$$

The first term on the right hand side describes the convective transport of the magnetic field; the second term results from using cylindrical coordinates. The third term describes the variation of the magnetic field, which is caused by electric current, Hall current and the diffusion flux by electron pressure. In Eq. 21 the magnetic flux density B_φ can be substituted by the stream function

$$\Psi = r B_\varphi . \tag{22}$$

For steady state conditions, the electric current is constant between two contour lines of the stream function Ψ. The conservation equation for the axial and radial magnetic field in vector potential formulation is given by

$$\frac{\partial A}{\partial t} = \frac{1}{\mu_0 \sigma} \mathrm{div}\left(\nabla A\right) + \vec{v} \times \vec{B} - \beta\left(\vec{j} \times \vec{B}\right) - \frac{A}{\mu_0 \sigma r^2}. \tag{23}$$

The components of the current density are computed by

$$\begin{aligned} j_r &= -\frac{1}{\mu_0 r} \frac{\partial \Psi}{\partial z}, \\ j_z &= \frac{1}{\mu_0 r} \frac{\partial \Psi}{\partial z} \quad \text{and} \\ j_\varphi &= \sigma\left(v_z B_r - v_r B_z\right) - \beta\sigma\left(j_z B_r - j_r B_z\right). \end{aligned} \tag{24}$$

IV. Computational Methods

For numerical simulations of AF-MPD thrusters the complex geometries of these devices have to be considered. Additionally, parametric optimization analyses require frequent changes in thruster geometries. Therefore, the computational domain is discretized using unstructured grids. The grid consists of triangles produced by an advancing front algorithm.[17,18] Based on these primary triangles, so-called dual cells are constructed. The corners of these dual cells are in the centers of mass of the primary triangles. [11,13] On cylindrical coordinates the dual cells represent toroidal control volumes which contain the average values of variables computed during the numerical simulations. By using adaptation techniques, the computational time can be reduced significantly.

The hyperbolic part of the conservation equations has to be solved by an adequate upwind scheme. In AF-MPD thrusters with three-dimensional magnetic fields the physical eigenvalues correspond to one entropy wave, two Alfvén waves and four magnetosonic waves (two slow and two fast). The choice of a numerical scheme is based on its accuracy and robustness. For example, Roe-type solvers are very accurate but not particularly robust for MPD calculations.[19] In addition, Roe solvers are computationally very expensive. The approach used here for the computation of the hyperbolic part of the conservation equations is a HLLE scheme.[19-21] The full Riemann solution at the cell faces is approximated by a single intermediate state bounded by two waves. Their wave speeds are Roe-averaged numerical approximations to the physical minimum and maximum wave speeds, which are the fast magnetosonic waves, for that particular Riemann problem. The intermediate state can be calculated by the condition of conservation.[22]

To achieve second order accuracy in space, all variables needed to compute the inviscid fluxes through the cell faces of the dual cells have to be linearly reconstructed. Within the scope of this work a second-order Weighted Essentially Non-Oscillatory (WENO) scheme is used.[11,23]

Independent of the discretization method used for the hyperbolic part of the conservation equations, the parabolic fluxes are computed by a central scheme. On unstructured grids simple central differences expressions used on

structured grids can not be applied. Therefore, according to Heiermann the fluxes are evaluated on each triangle with Cramer's rule to achieve a quasi-central scheme.[11] All other differentials needed for the calculations are computed by the least-square method.

To achieve a steady-state solution, time integration is done by explicit, first-order, randomized local time steps.[11]

A. Boundary conditions

On the inlet boundary the mass flow rate and temperature are specified and kept constant by a numerical flow controller.[11] On solid walls the no-slip boundary condition is implemented. Flow velocity is set to zero, heavy particle temperature is set to a specified wall temperature and electrons are assumed to behave adiabatic. On the outlet boundary subsonic or supersonic outflow conditions are used depending on the local Mach number. It is also possible to simulate recirculation of remaining gas in a vacuum tank. If the plasma velocity vector points inwards at the outlet boundary, predefined ambient conditions are used.

The electric field is assumed to be perpendicular to the electrode surfaces. On boundary cells ω upstream from the electrodes the value of the stream function Ψ is defined by Ampère's law with the discharge current I_A:

$$\Psi_\omega = \frac{\mu_0 I_A}{2\pi}. \tag{25}$$

On boundary cells downstream from the electrodes the stream function is zero.

According to Jackson[16] and Heiermann[24] the vector potential A at cell ω caused by the solenoidal coil current I_c and by induced azimuthal current density j_φ is given by

$$A_\omega = I_c \underbrace{\frac{\mu_0}{2\pi}\sum_{c=1}^{N_{coil}}\left[\sqrt{\frac{r_c}{r_{m,\omega}}}G(k)\right]}_{\text{Preprocessing}} + \frac{\mu_0}{2\pi}\sum_{i=1,i\neq\omega}^{N_{cell}}\left[\underbrace{\sqrt{\frac{r_c}{r_{m,\omega}}}\Delta A_i G(k)}_{\text{Preprocessing}} j_{\varphi,i}\right] \tag{26}$$

with the definitions

$$G(k) = \frac{\left(2-k^2\right)K(k) - 2E(k)}{k},$$
$$k = \sqrt{\frac{4 r_c r_{m,\omega}}{\left(r_c + r_{m,\omega}\right)^2 + \left(z_{m,\omega} - z_c\right)^2}} \tag{27}$$

and the elliptic integrals

$$K(k) = \int_0^{\pi/2} \frac{d\varphi}{\sqrt{1-k^2\sin^2\varphi}},$$
$$E(k) = \int_0^{\pi/2} \sqrt{1-k^2\sin^2\varphi}\, d\varphi. \tag{28}$$

These elliptic integrals are solved by Gauß-Legendre integration.[24,25] In Eq. 26 and 27 the solenoidal coil is modelled as an array of ring-shaped windings. The coordinates r_c and z_c of each winding can be specified separately, so complicated coil configurations can be implemented. The computation of the elliptic integrals is computationally very expensive. Therefore, as indicated in Eq. 26, the calculation of the geometric factors influenced by the elliptic integrals is done once before a numerical simulation is started for a given thruster and coil geometry.

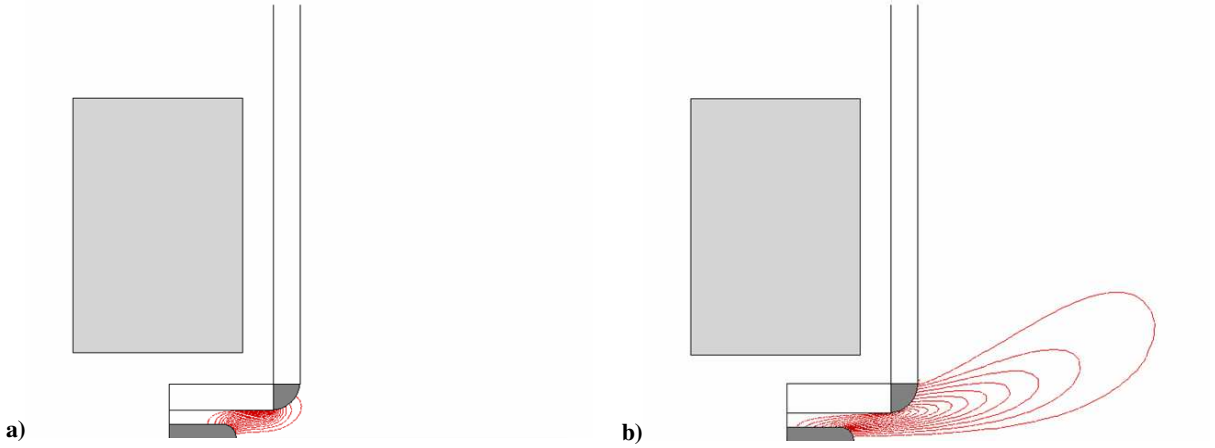

Figure 2. Current distribution Ψ : a) applied magnetic field strength is zero, and b) applied magnetic field strength is $B = 0.6\,\mathrm{T}$ at cathode tip.

V. Numerical Results

A. Anisotropic electric conductivity

In order to investigate the current distribution caused by the applied magnetic field, calculations have been made for the thruster geometry shown in Fig. 2. Within these calculations the plasma velocity has been kept to zero, the heavy particle density has been set to $\rho = 2.4 \cdot 10^{-4}\ \mathrm{kg/m^3}$, the heavy particle temperature has been held constant at $T_h = 1000\,\mathrm{K}$, the electron temperature at $T_e = 10000\,\mathrm{K}$ and the heavy particle pressure has been set to $p_h = 50\,\mathrm{Pa}$. With the assumption of chemical equilibrium, the particle densities of the ionized species and the transport coefficients have been calculated. Within these calculations the coil for applying the external magnetic field consisted of 15 layers of windings. Each layer had 10 windings. The discharge current was held constant at $I_A = 80\,\mathrm{A}$. Figure 2.a) shows the current distribution Ψ in the self-field MPD case without an external magnetic field; in Fig. 2.b) the current distribution is given for an applied magnetic field of $B = 0.6\,\mathrm{T}$ at the cathode tip. By increasing the external magnetic field strength, the current streamlines are extended downstream from the thruster. This is induced by the "magnetic nozzle effect", i.e. the anisotropic electric conductivity, as mentioned in section II. Within the system of conservation equations the anisotropy is caused by the Hall term of the magnetic induction equation Eq. 21.

B. AF-MPD thruster simulations

Numerical simulations of an AF-MPD thruster have been accomplished with a thruster geometry aligned with the laboratory model described in section VI and an outer anode diameter of $\varnothing_A = 40\,\mathrm{mm}$. At the investigated thruster geometry the propellant is fed through the hollow cathode with the mass flow $\dot{m}_C$ and through the annular gap near the anode with the mass flow $\dot{m}_A$. Within these calculations the full system of conservation equations for an argon plasma flow in thermal and chemical non-equilibrium has been used, which is described in section III. Figures 3 to 7 show the results for the operating parameters summarized in Table 1. The external magnetic field was created by a coil, which consisted of 15 layers of windings and 10 windings in each layer. At a coil current of $I_C = 100\,\mathrm{A}$ the resulting applied magnetic field at the cathode tip became $B = 0.12\,\mathrm{T}$**.** For the results shown the discharge current was $I_A = 80\,\mathrm{A}$, the cathode gas flow $\dot{m}_C = 5\,\frac{\mathrm{mg}}{\mathrm{s}}$ and the anode gas flow $\dot{m}_A = 2\,\frac{\mathrm{mg}}{\mathrm{s}}$.

Table 1. Operating parameters for numerical simulation; results shown in Fig. 3 to Fig. 7.

Outer diameter of anode:	$\varnothing_A = 40$ mm
Cathode mass flow rate:	$\dot{m}_C = 5\,\frac{\text{mg}}{\text{s}}$
Anode mass flow rate:	$\dot{m}_A = 2\,\frac{\text{mg}}{\text{s}}$
Discharge current:	$I_A = 80$ A
Coil geometry: 15 layers with 10 windings in each layer (150 windings altogether).	
Coil current:	$I_C = 100$ A
Applied magnetic field:	$B = 0.12$ T

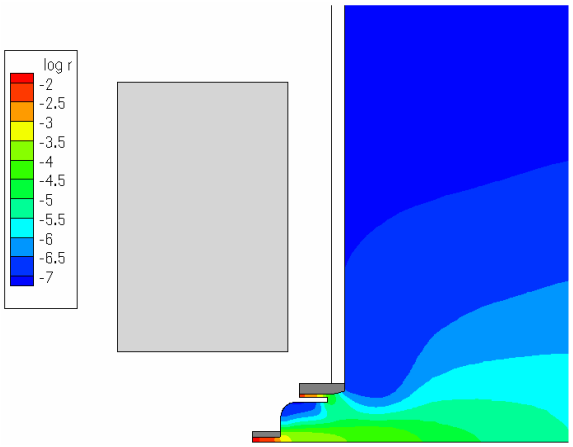

Figure 3. Heavy particle density $\log_{10}\rho$.

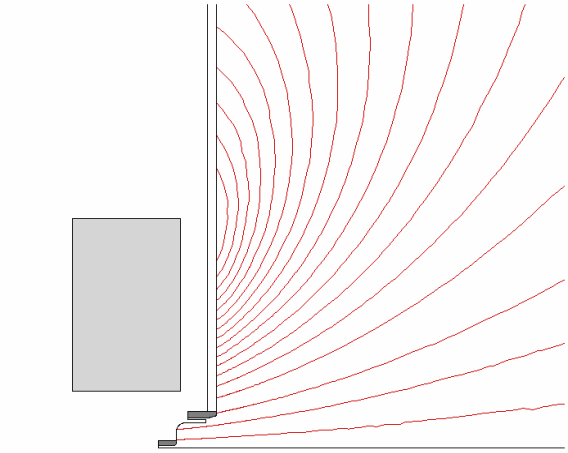

Figure 4. Field lines of the applied magnetic field.

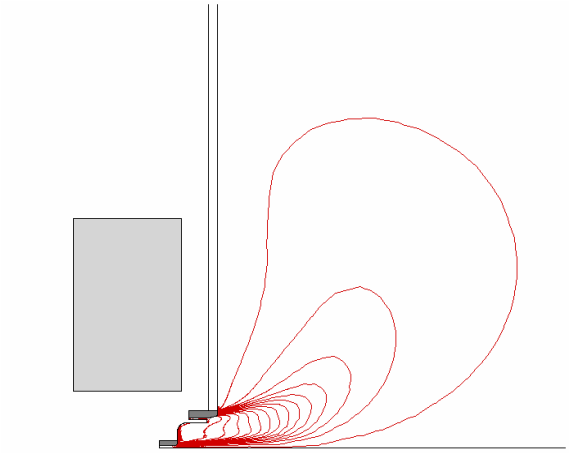

Figure 5. Current distribution Ψ.

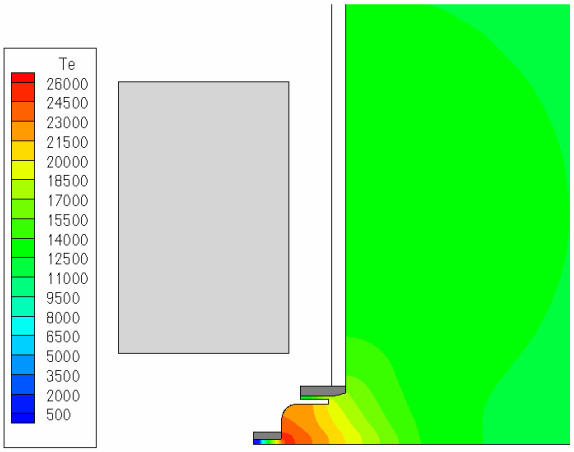

Figure 6. Electron temperature T_e.

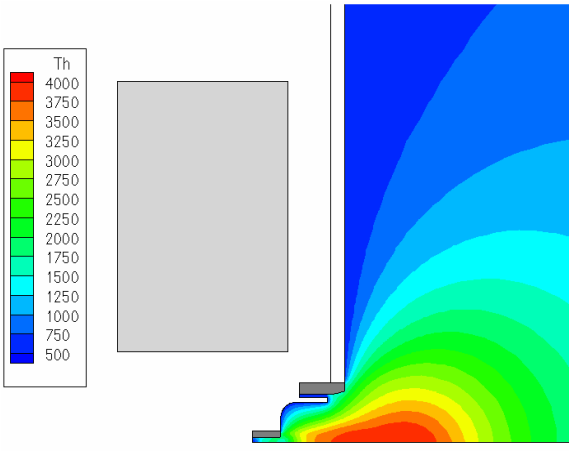

Figure 7. Heavy particle temperature T_h.

Figure 3 shows the distribution of heavy particle density $\log_{10}\rho$. With increasing applied magnetic field an area of low density appears inside the thruster, and the constriction of the plasma flow in front of the anode gets stronger. The field lines of the applied magnetic field are shown in Fig. 4. In Fig. 5 the current distribution Ψ is given. The contour lines of the current distribution show perturbations in front of the electrodes which rise with increasing strength of the applied magnetic field. Especially for the thruster geometry shown here these perturbations become

obvious inside the thruster also. The perturbations inside the thruster increase as the particle density decreases with stronger applied magnetic fields. This can be traced back to the Hall term of the azimuthal induction equation Eq. 21, which is inversely proportional to electron density. With increasing values of the applied magnetic field this leads to instabilities in the numerical calculations, which have to be investigated further.

The distribution of electron temperature T_e is shown in Fig. 6, and the distribution of the heavy particle temperature T_h is given in Fig. 7. The non-equilibrium between electrons and heavy particles is clearly noticeable. As a result of the low particle density, the collision frequencies and the energy exchange between the particles are low. Because of their low mass and high mobility, the electrons are assumed to carry the electric current in the plasma. Therefore, the electron temperature is increased by Ohmic heating. Only a small part of the energy is transferred to the heavy particles.

VI. Experimental Investigations

The AF-MPD thruster DFVLR-X16 developed at DLR Stuttgart is still one of the most effective thrusters in the power range 10-20 kW with noble gas as propellant today.[8] Therefore, the X16 thruster design has been used as a starting point for the development of the AF-MPD laboratory model at IRS. The design of the IRS thruster model, which is currently under construction, is shown in Fig. 8. The laboratory thruster has an outer anode diameter of 40 mm. The total length is 355 mm.

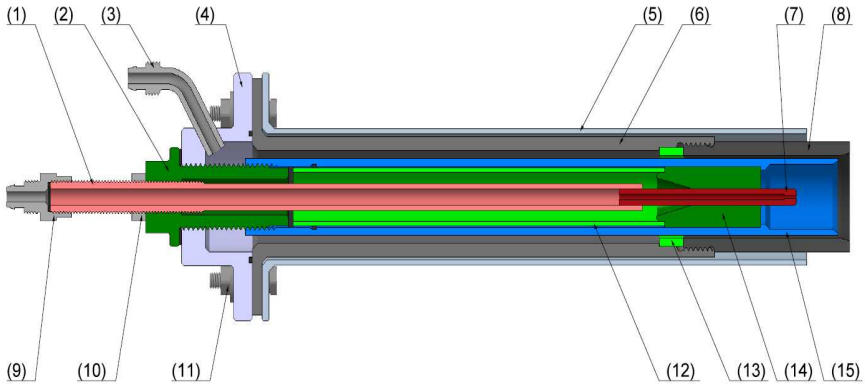

(1): Cathode (Cu)
(2): Cathode mounting (PEEK)
(3): Gas connector
(4): Structural connection (Steel)
(5): Radiation shield (Steel)
(6): Anode (TZM)
(7): Cathode (WT20)
(8): Anode (WT20)
(9): Gas connector
(10): Locknut
(11): Bolted connection
(12): Insulator (Macor)
(13): Insulator (BN)
(14): Insulator (BN)
(15): Neutral liner (TZM)

Figure 8. Current design of the AF-MPD laboratory thruster at IRS without magnet.

Several design criteria have been taken into account during the development. The thruster is radiation-cooled, which not only simplifies the design but also allows further development of the thruster with regard to a flight model. The thruster has two independent gas inlets through a hollow cathode and through an annular gap near the anode. The gas delivery near the anode should prevent the depletion of density and charge carriers in the anode zone. This reduces instabilities during operation and could also improve efficiency.[26]

The thruster has a modular design, which allows changes in electrode geometry and magnetic field configuration as a consequence of numerical and experimental results. The assembly of the thruster is flexible. The anode and cathode can be easily detached without disassembling the entire thruster. Variation of the distance between cathode tip and anode exit plane, and also of the distance between neutral liner exit plane and anode exit plane is possible to find an optimized thruster configuration.

The layout of the coil, which will be used for creating the applied magnetic field for the experimental investigations, is only limited by the outer diameter of the radiation shield. The final design of the coil has not been deter-

mined yet. Based on numerical and experimental results, the configuration of the coil can be adapted. The investigation of permanent magnets is also possible with the laboratory thruster in future with regard to a flight model.

The intention of the experimental investigations at IRS is to determine the operation and performance parameters of the AF-MPD thruster. The experimental investigations allow a judgement of the quality of the numerical simulation program SAMSA. Based on numerical and experimental results, further optimizations of electrode geometries and magnetic field configurations should be possible.

VII. Conclusion

The numerical simulation program SAMSA as described in this paper allows detailed simulations of argon plasma flows in AF-MPD thrusters. Parametric analyses of electrode configuration, nozzle geometry and configuration of the solenoidal coils are possible. These analyses are eased by using a finite volume scheme on unstructured grids, which allows for fast customization to various, complicated thruster geometries. In addition, the configuration of the solenoidal coil can be changed with minimum effort. The calculations for the investigated AF-MPD thruster geometries show perturbations in the current stream lines at strong applied magnetic fields. This leads to instabilities in the numerical simulations, which will be examined further.

A laboratory model of an AF-MPD thruster has been designed and is currently under construction at IRS. The laboratory model will be tested at IRS facilities with regard to its operating and performance parameters. The comparison of numerical and experimental results should lead to a better understanding of the physical processes in AF-MPD thrusters and an optimized thruster design.

Acknowledgments

The authors wish to thank the German Research Foundation DFG (Deutsche Forschungsgemeinschaft) for the financial support through the project "Numerische Simulation zur Auslegung eines magnetoplasmadynamischen Triebwerks mit überlagertem koaxialem Magnetfeld" (Au 88/25-1).

References

[1]Kurtz, H., Auweter-Kurtz, M., and Heiermann, J., "Magnetoplasmadynamic Thrusters with Coaxial Applied Field," Propulsion 2000, Final Version, IRS-02-P13, 2002.

[2]Krülle, G., "On the Dynamics of the Axisymmetric Magnetoplasmadynamic Accelerator (MPD Thruster) with Applied Magnetic Field," Ph.D. Dissertation, Technical University of Munich, DLR FB-74-56, DFVLR, Munich, Germany, 1974.

[3]Krülle, G., and Zeyfang, E., "Preliminary Conclusions of Continuous Applied Field Electrodynamic Thruster Research at DFVLR," *AIAA Paper* 75-417, 1975.

[4]Sovey, J.S., and Mantenieks, M.A., "Performance and Lifetime Assessment of Magnetoplasmadynamic Arc Thruster Technology," *Journal of Propulsion and Power*, Vol. 7, No. 1, 1991.

[5]Tikhonov, V., Semenikhin, S., Brophy, J.R., and Polk, J.E., "The Experimental Performances of the 100 kW Li MPD Thruster with External Magnetic Field," *International Electric Propulsion Conference*, IEPC 95-105, 1995.

[6]Sasoh, A., and Arakawa, Y., "Steady-State Permanent Magnet Magnetoplasmadynamic Thruster," *Journal of Propulsion and Power*, Vol. 5, No. 3, 1989.

[7]Sasoh, A., and Arakawa, Y., "Thrust Formula for Applied-Field Magnetoplasmadynamic Thrusters Derived from Energy Conservation Equation," *Journal of Propulsion and Power*, Vol. 11, No. 2, 1995.

[8]Krülle, G., Auweter-Kurtz, M., and Sasoh, A., "Technology and Application Aspects of Applied Field Magnetoplasmadynamic Propulsion," *Journal of Propulsion and Power*, Vol. 14, No. 5, 1998.

[9]Krülle, G., "Theoretical Treatment of Current, Mass Flow, and Related Distributions in MPD Plumes," *AIAA Paper* 72-501, 1972.

[10]Auweter-Kurtz, M., Kurtz, H., "MATEX Magnetoplasmadynamic Thruster Experiment," First Symposium on the Utilization of the International Space Station, pp. 501-504, ESOC, Darmstadt, Germany, 1996.

[11]Heiermann, J., "A Finite Volume Method for the Solution of Magnetoplasmadynamic Conservation Equations," Doctoral Thesis, Institut für Raumfahrtsysteme, Universität Stuttgart, Stuttgart, Germany, 2002.

[12]Auweter-Kurtz, M., *Lichtbogenantriebe für Weltraumaufgaben*, B.G. Teubner-Verlag, Stuttgart, Germany, 1992.

[13]Heiermann, J., and Auweter-Kurtz, M., "Numerical and Experimental Investigation of the Current Distribution in Self-Field MPD Thrusters," *AIAA Paper* 2001-3498, 2001.

[14]Trostel, R., *Vektor- und Tensoranalysis*, Vieweg-Verlag, Wiesbaden, Germany, 1997.

[15]Cap, F., *Lehrbuch der Plasmaphysik und Magnetohydrodynamik*, Springer-Verlag, Wien, Austria, 1994.

[16]Jackson, J.D., *Classical Electrodynamics*, 2nd ed., John Wiley and Sons, 1975.

[17]Boie, C., Auweter-Kurtz, M., Kaeppeler, H.J., and Sleziona, P.C., "Numerical Simulation of MPD Thrusters on Adaptive Unstructured Mesh," *Computational Fluid Dynamics '94*, edited by S. Wagner, E.A. Hirschel, J. Periaux and R. Piva, John Wiley and Sons, 1994.

[18]Boie, C. „Numerische Simulation magnetoplasmadynamischer Eigenfeldtriebwerke mit hochauflösenden adaptiven Verfahren," Doctoral Thesis, Institut für Raumfahrtsysteme, Fakultät Luft- und Raumfahrttechnik, Universität Stuttgart, Stuttgart, 1999.

[19]Linde, T.J., "A Three-Dimensional Adaptive Multifluid MHD Model of the Heliosphere," Ph.D. Dissertation, University of Michigan, 1998.

[20]Harten, A., Lax, P.D., and van Leer, B., "On Upstream Differencing and Godunov-Type Schemes for Hyperbolic Conservation Laws," *SIAM Review*, Vol. 25, No. 1, 1983.

[21]Einfeldt, B., "On Godunov-Type Methods for Gas Dynamics," *SIAM Journal on Numerical Analysis*, Vol. 25, No. 2, 1988.

[22]LeVeque, R.J., "Nonlinear Conservation Laws and Finite Volume Methods for Astrophysical Fluid Flow," *Computational Methods for Astrophysical Fluid Flow*, edited by O. Steiner and A. Gautschy, Springer-Verlag, 1998.

[23]Friedrich, O., "Weighted Essentially Non-Oscillatory Schemes for the Interpolation of Mean Values on Unstructured Grids," *Journal of Computational Physics*, Vol. 144, No.1, 1998.

[24]Heiermann, J., Auweter-Kurtz, M., Lenzner, S., and Sleziona, P.C., „Erstellung eines elektrodynamischen Programmmoduls zur Modellierung der Plasmaströmung in einem HF-Generator mit Hilfe der Methode der Finiten Differenzen auf einem strukturiert krummlinigen Netz," Diploma Thesis, IRS-97-S25, Institut für Raumfahrtsysteme, Universität Stuttgart, 1997; DGLR-JT98-196, DGLR Jahrbuch, ISSN 0070-4083, pp. 923-928, 1998.

[25]Banerjee, P.K., *The Boundary Element Methods in Engineering*, McGraw-Hill, 1994.

[26]Kurtz, H., "Integrale Messungen an einem axialsymmetrischen elektromagnetischen Plasmabeschleuniger (Triebwerksmodell X-13)", Diploma Thesis, Institut für Raumfahrtsysteme, Universität Stuttgart, 1971.